


# Modal analysis of dielectric barrier discharge-based argon cold plasma jet

cambridge.org/lpb

G. Divya Deepak<sup>1</sup> , N. K. Joshi<sup>2</sup> and Ram Prakash<sup>3</sup>

## Research Article

**Cite this article:** Deepak GD, Joshi NK, Prakash R (2020). Modal analysis of dielectric barrier discharge-based argon cold plasma jet. *Laser and Particle Beams* **38**, 229–238. <https://doi.org/10.1017/S0263034620000294>

Received: 23 January 2020  
Revised: 16 June 2020  
Accepted: 25 August 2020  
First published online: 9 October 2020

### Key words:

Atmospheric pressure plasma jet; dielectric barrier discharge; supply frequency; supply voltage

### Author for correspondence:

G. Divya Deepak, Department of Mechanical Engineering, Alliance University, Anekal, Bangalore 562106, India.  
E-mail: [divyadeepak77@gmail.com](mailto:divyadeepak77@gmail.com)

<sup>1</sup>Department of Mechanical Engineering, Alliance University, Anekal, Bangalore 562106, India; <sup>2</sup>Department of Nuclear Science and Technology, Mody University of Science and Technology, Lakshmangarh, Rajasthan 32311, India and <sup>3</sup>Department of Physics, IIT, Jodhpur, Rajasthan 342037, India

### Abstract

In this study, an atmospheric pressure dielectric barrier discharge-based argon plasma jet has been modeled using COMSOL Multiphysics, which is based on the finite element method. The fluid dynamics and plasma modules of COMSOL Multiphysics code have been used for the modeling of the plasma jet. The plasma parameters, such as electron density, electron temperature, and electrical potential, have been examined by varying the electrical parameters, that is, supply voltage and supply frequency for both cases of static and with the flow of argon gas. The argon gas flow rate was fixed at 1 l/min. Ring electrode arrangement is subjected to a range of supply frequencies (10–25 kHz) and supply voltages (3.5–6 kV). The experimental results of the ring electrode configuration have been compared with the simulation analysis results. These results help in establishing an optimized operating range of the dielectric barrier discharge-based cold plasma jet in the glow discharge regime without arcing phenomenon. For the applied voltage and supply frequency parameters examined in this work, the discharge was found to be consistently homogeneous and displayed the characteristics of atmospheric pressure glow discharge.

## Introduction

Atmospheric pressure plasma jets (APPJs) based on dielectric barrier discharge (DBD) have shown significant potential for implementing them in low-temperature gas processing applications at atmospheric pressure, thereby eliminating the need for a vacuum chamber (Jeong *et al.*, 1998; Stoffels *et al.*, 2002, 2003; Benhansour *et al.*, 2004; Deng *et al.*, 2005; Walsh *et al.*, 2006; Divya Deepak *et al.*, 2018a, 2018b). These plasma jets are close to room temperature, and hence, popularly referred to as atmospheric pressure cold plasma jets (APCPJs) (Deng *et al.*, 2005). The APCPJs have acquired considerable attention due to their pivotal role in various plasma processing applications. The other intriguing feature of cold plasma jets is that they are not restricted by electrodes (Eliasson and Kogelchitz, 1991; Kruger *et al.*, 1997; Sladek *et al.*, 2004) APCPJs have further been utilized in various biomedical and technological applications (Schutze *et al.*, 1998; Xu, 2001; Duan *et al.*, 2005; Roth *et al.*, 2007; Xu *et al.*, 2008; Kim *et al.*, 2010). The most imperative property of this plasma type is that it functions close to room temperature and also lets the treatment of uneven surfaces with the minor depth of penetration. Various researchers (Frame *et al.*, 1997; Selwyn *et al.*, 2001; Chirokov *et al.*, 2005; Becker *et al.*, 2006). Raizer (1991) had elaborated upon the fundamental discharge phenomenon of DBD-based plasmas. It is mentioned that in case of air gaps produced by the plane electrodes if  $p \cdot d > 5000$  Torr cm, steamer breakdown is employed and Townsend mechanism of avalanche multiplication is implemented for  $p \cdot d < 200$  Torr cm, where the distance between the electrodes is denoted by  $d$  and  $p$ , refers to the pressure. Streamer breakdown is characteristic of comparatively large air gaps. As the value of  $p \cdot d$  is less than 200 Torr cm for the ring electrode structure mentioned in this current research work; therefore, this mechanism of discharge is mostly directed by a Townsend breakdown mechanism which is related to the expansion of multiple avalanches. The ring electrode structure has been studied here to optimize the operational factors (supply frequency, supply voltage) to produce cold plasma jets that have long jet lengths. This electrode configuration may be used for possible technological applications.

The ring electrode structure mentioned in the current research work fulfills all the essential conditions for its applications in biomedical applications, which are low gas temperature, rich active species, no arcing, and jet ejecting in air. Teschke *et al.* (2005) examined an APPJ using an intensified charge-coupled device (ICCD) camera. It is found that the formation of APPJ is chiefly an electrical phenomenon and not related to flow. Maximum power of 4 W was consumed by this device, while the ring electrode structure mentioned in this research paper has a maximum power consumption of only 1.27 W. Further, Lu and Laroussi (2006) examined the atmospheric pressure dynamics produced by sub-microsecond pulses with the help of  $V-I$

© The Author(s) 2020. Published by Cambridge University Press

**CAMBRIDGE**  
UNIVERSITY PRESS

characteristics and also used CCD camera for examining the spatial and temporal evolutions of the plasma within the discharge chamber. Honga and Uhm (2006) produced microplasma jet using nitrogen gas at atmospheric pressure with the help of two aluminum disks in which the gas temperature was found to be less than 3000 K and it was recommended to be implemented for medical applications. Lu *et al.* (2008) created an 11 cm cold plasma jet using an ac power supply (kHz) for technological applications; however, optimization of electrical parameters (supply frequency and supply voltage) of the device had not been done. Nie *et al.* (2008) produced a plasma jet of argon gas with the help of the tungsten pin electrode pair which was 2.5 mm apart. Among these, one of the tungsten pin electrodes had been kept at a floating potential. The effect of the applied potential and velocity of flow on plasma jet was investigated; however, the power consumed by the plasma jet was not estimated. Pal *et al.* (2012) examined the multiple-peak discharge occurrence via an equivalent circuit. Radu *et al.* (2003) investigated an APPJ in the DBD reactor under variable experimental conditions (electric field intensity, gap length, and supply frequency) which assisted them in the electrical characterization of the DBD. Kim *et al.* (2009) produced plasma based on argon gas with the help of a piezo transducer which had a maximum power consumption of 2 W.

Hong Yi *et al.* (2013) was successful in generating a DBD-based plasma jet using argon gas by implementing a screw ring-ring electrodes, here the emission spectra of argon had been investigated to find out the physical parameters (supply voltage and frequency) of the discharge, like, the temperature of gas and consumption of power. Joh *et al.* (2014) created a plasma jet based on helium with the help of pin-shaped electrode where the effects of nozzle shape, electrode materials, and grounded ring electrode on the plasma were investigated; however, the particulars about the consumption of power by the device at different supply voltages and frequencies was not mentioned. Shashurin and Keidar (2015) examine the research work done in the domain of cold atmospheric pressure plasma jets (C-APPJs) with specific emphasis on experimental methods. Divya Deepak *et al.* (2016) implemented ring electrode configuration to investigate DBD-based argon cold plasma jets and characterized them electrically. Divya Deepak *et al.* (2017) produced a cold plasma jet using a floating helix electrode configuration which had a power consumption of the range of few mW. Kelly and Turner (2011) investigated an atmospheric pressure plasma which was based on alternating current and generated a two-dimensional (2D) fluid model of the same. Tendero *et al.* (2006) had completed the modeling of a DBD-based reactor with the incorporation of gas flow using COMSOL Multiphysics 5.2a. RF-based plasma needle modeling had been completed using a fluid model having a small fraction of N<sub>2</sub> and He by Sakiyama and Graves (2006).

Preliminary work on DBD-based modeling was only completed for the static discharge of gas. Modeling of streamer like APPJ was completed by Naidis (2012). The fluid model developed by Gadkari *et al.* (2017) using COMSOL Multiphysics for a partially packed DBD-based plasma reactor that was based on pure He. Only a few studies have been done for modeling of DBD incorporating the flow of gas. Both electrical characterization and modeling of a DBD-based APPJ using argon gas in the pin electrode geometry has been completed by Divya Deepak *et al.* (2018a, 2018b). This paper focuses on DBD-based APPJs including the flow of argon gas using fluid dynamics and the plasma module of COMSOL Multiphysics (Divya Deepak *et al.*, 2018a,

2018b). COMSOL is multiphysics software is based on a finite element method (FEM). It contains a plasma module in which we can perform 1D, 2D, and 3D modeling, and simulation of APPJs generated using different electrode configurations. Each module of the COMSOL Multiphysics has a defined group of domain equations that are detailed to describe the physics of the process. The COMSOL modules contain all the attributes that are essential for modeling plasma discharge, starting with a Boltzmann Equation, 2-Term Approximation solver that estimates transport properties of source coefficients and electrons from a set of electron impact collision cross-sections (Hagelaar and Pitchford, 2005).

In this paper, modeling work has been carried out for DBD-based APPJs for a ring electrode configuration in both static discharge condition and with the flow of Ar gas. The effect of supply voltage and frequency on the plasma parameters like electron density, electron temperature, and the electrical potential of the DBD-based APPJs has been analyzed with the help of simulation results obtained using COMSOL Multiphysics software. The simulation program stops at the instant of discharge initiation due to convergence of the iterative algorithm of electron energy distribution function (EEDF; Hagelaar and Pitchford, 2005) and does not provide the results of plasma parameters (electron density, electron temperature, and electrical potential) during the plasma discharge process (Divya Deepak *et al.*, 2018a, 2018b). It is also imperative to mention that in this research work, the plasma diagnostics has not been done during the experiments to determine plasma density and temperature.

## Geometry and experimental setup

The experimental setup of ring electrode geometry is presented in Figure 1.

The double ring electrode arrangement is used in this study consists of a long quartz tube with a nozzle, as shown in Figure 1. The nozzle of the quartz tube has two metal sleeves wound on it which acts as the ring electrodes. It is imperative to note that the green metal sleeve colored is connected to the pulsed power supply, while the other red-colored metal sleeve is grounded. The outer diameter and length of the quartz tube are 25 and 155 mm, respectively. The quartz tube thickness is 1.5 mm. Argon gas flows through the inlet of the quartz tube indicated as 1 (see Fig. 2) with an inner diameter is 22 mm. The outer diameter of the nozzle outlet is 6 mm, while its inner diameter is 3 mm which has been indicated as 2 (see Fig. 2). The length of the ring electrodes (indicated as 3) (see Fig. 2) and thickness are 18 and 4 mm, respectively. The ring electrodes indicated as 3 are separated by a distance of 3 mm and are clearly shown in Figure 2. A quartz sleeve of 7 mm outer diameter and 15 mm length was placed on the nozzle of the quartz tube (see Fig. 2) to observe the length of the plasma jet without the effect of the surrounding air.

A high-voltage probe (Tektronix P 6015 A) (Bandwidth 0–75 MHz) was used to measure the applied voltage. The applied currents were measured using Rogowski-type Pearson current monitor (Model 110) (0.1 V/A, 1 Hz–20 MHz, 20 ns usable rise time) which was connected to a digital storage oscilloscope (Tektronix DPO 4054, bandwidth: 500 MHz). Experiments were implemented using argon gas with a gas flow rate of 1 l/min in a hermetically sealed setup at atmospheric pressure and the further same gas flow rate was used for simulation analysis also. A typical cold plasma jet produced using ring electrode geometry is depicted in Figure 3.

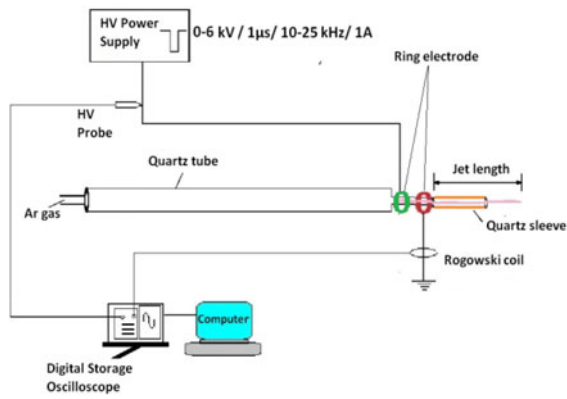


Fig. 1. Experimental setup of ring electrode-based APPJ.

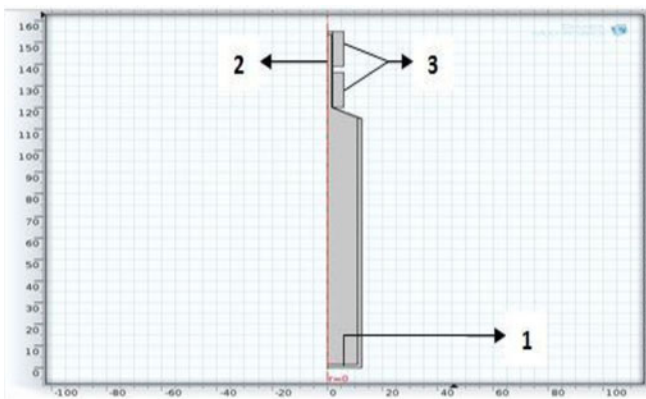


Fig. 2. Geometry of ring electrode-based APPJ.



Fig. 3. Cold plasma jet generated using a ring electrode configuration (Divya Deepak *et al.*, 2016).

**Governing equations for discharge simulations**

The mean electron energy and electron density are computed by solving a pair of drift-diffusion equations for the mean electron energy and electron density.

$$\frac{\partial}{\partial t}(n_e) + \nabla \cdot [-n_e(\mu_e \cdot E) - D_e \cdot \nabla n_e] = R_e \tag{1}$$

$$\frac{\partial}{\partial t}(n_e) + \nabla \cdot [-n_e(\mu_e \cdot E) - D_e \cdot \nabla n_e] + E \cdot \Gamma_e = R_e \tag{2}$$

$$\Gamma_e = -(\mu_e \cdot E)n_e - D_e \cdot \nabla n_e \tag{3}$$

Here,  $n_e$  is the electron density,  $n_e$  is the electron energy density,  $\mu_e$  is the electron mobility,  $\mu_e$  is the electron energy mobility,  $E$  is the electric field,  $R_e$  is the electron rate expression,  $R_e$  is the energy loss/gain due to inelastic collisions,  $D_e$  is the diffusion coefficient of electrons,  $D_e$  is the electron energy diffusivity, and  $\Gamma_e$  is the electron flux.

Plasma chemistry using rate coefficients is used to determine the source coefficient in the equations mentioned above.

In the case of rate coefficients, the electron source term is specified by

$$R_e = \sum_{j=1}^M x_j k_j N_n n_e \tag{4}$$

where  $M$  denotes the reactions that contribute to the growth or decay of electron density.

The mole fraction of the target species for reaction  $j$  is given by  $x_j$ , the rate coefficient for reaction  $j$  is given as  $k_j$ , and the total neutral number density is  $N_n$ . The electron energy loss is obtained by summing entire collisional energy loss over all reactions and written as follows:

$$R_e = \sum_{j=1}^P x_j k_j N_n n_e \Delta \epsilon_j \tag{5}$$

where  $\Delta \epsilon_j$  is the energy loss from reaction  $j$  and  $P$  denotes the inelastic electron-neutral collisions. In general,  $P \gg M$ . The rate coefficients can be computed from cross-section data by the following integral

$$k_j = \gamma \int_0^\infty \epsilon \sigma_j(\epsilon) f(\epsilon) d\epsilon \tag{6}$$

where  $\gamma = (2q/m_e)^{1/2}$ ,  $m_e$  is the mass of an electron,  $\epsilon$  is energy (V),  $f$  is the electron energy distribution function, and  $\sigma_j$  is the cross section of collision.

In this case, the EEDF is assumed Maxwellian because in DBD-based plasmas, the degree of ionization is high and as a consequence, the electron-electron collisions drive the distribution toward the Maxwellian shape. The EEDF can be computed by solving the Boltzmann equation. The evolution of the distribution function,  $f$ , in a six-dimensional phase space is expressed as follows:

$$\frac{\partial f}{\partial t} + v \Delta f - \left(\frac{eE}{m}\right) \nabla_v = C[f] \tag{7}$$

where  $f$  is the electron distribution function,  $v$  is the velocity coordinate,  $e$  is the elementary charge,  $m$  is the electron mass,  $E$  is the electric field,  $\nabla_v$  is the velocity-gradient operator, and  $C$  represents the rate of change in  $f$  due to collisions. In the code, EEDF is assumed to be almost spherically symmetric, so the series can be truncated after the second term (a so-called two-term approximation) (Divya Deepak *et al.*, 2018a, 2018b). An anisotropic perturbation is also applied due to inelastic collisions under consideration. A detailed explanation of two-term approximation is given elsewhere (Hagelaar and Pitchford, 2005).

The electron diffusivity, energy mobility, and energy diffusivity are calculated from the electron mobility using the following

equations:

$$D_e = \mu_e T_e, \quad \mu_e = \left(\frac{5}{3}\right) \mu_e, \quad D_e = \mu_e T_e \quad (8)$$

where  $T_e$  is the temperature of the electron.

$$\text{Mean electron energy} \rightarrow \varepsilon = \frac{n_e}{n_e} \quad (9)$$

$$\text{Electron temperature } T_e = \left(\frac{2}{3}\right) \rightarrow \varepsilon \quad (10)$$

and electrostatic potential is given by the expression,

$$-\nabla \varepsilon_0 \cdot \varepsilon_r \nabla V = \rho \quad (11)$$

where  $\rho$  is the space charge density and  $V$  is the applied sinusoidal electrical potential (Hagelaar and Pitchford, 2005).

### Governing equations flow simulations

In this simulation study, the effect of the argon gas flow rate has been analyzed for the electron density and electron temperature again using COMSOL 5.2a. The fluid dynamics module contains equations, volume forces, and boundary conditions that are essential for modeling freely moving fluids employing the Navier–Stokes equations and solve for the pressure and the velocity field. The laminar flow interface is used primarily to model flows of comparably low Reynolds number. The interface solves the Navier–Stokes equations, for incompressible and weakly compressible flows (Divya Deepak et al., 2018a, 2018b). The single-phase fluid-flow interfaces are computed using Navier–Stokes equations, as mentioned below:

$$\frac{\partial \rho}{\partial t} + \nabla \cdot (\rho u) = 0 \quad (12)$$

$$\frac{\rho \partial u}{\partial t} + \rho(u \cdot \nabla)u = \nabla \cdot [-pI + \tau] + F \quad (13)$$

$$\begin{aligned} \rho C_p \left( \frac{\partial T}{\partial t} + (u \cdot \nabla)T \right) &= -(\nabla \cdot q) + \tau : S - \left( \frac{T}{\rho} \right) \cdot \left( \frac{\partial \rho}{\partial t} \right) \\ &\times \left( \frac{\partial p}{\partial t} \right) + (u \cdot \nabla)p + Q \end{aligned} \quad (14)$$

$$S = 1/2(\nabla u + (\nabla u)^T) \quad (15)$$

$$\tau = 2\mu S - 2/3\mu(\nabla \cdot u)I \quad (16)$$

Here, density is given as  $\rho$ ,  $\tau$  is the viscous stress tensor,  $u$  is the velocity vector,  $p$  is the pressure,  $I$  is the identity matrix,  $F$  is the volume force vector,  $T$  is the absolute temperature,  $C_p$  is the specific heat capacity at constant pressure,  $q$  is the heat flux vector,  $S$  is the strain-rate tensor, and  $Q$  contains the heat sources. A contraction between tensors ( $S$  and  $\tau$ ) is denoted by operator “:” and is denoted as

$$S:\tau = \sum_n \sum_m S_{nm} \tau_{nm} \quad (17)$$

### Boundary conditions

Electrons are lost to the wall because of the random movement in the interval of a few mean free paths of the wall and some electrons are acquired due to secondary emission, thus ensuing in the boundary condition for the electron flux:

$$-n\Gamma_e = ((1/2)v_e)n_e - \sum_p \gamma_p(\Gamma_p n) \quad (18)$$

and the electron energy flux is computed as

$$-n\Gamma_\varepsilon = ((5/6)v_e)n_\varepsilon - \sum_p \varepsilon_p \gamma_p(\Gamma_p n) \quad (19)$$

The electrical potential at the external boundary of the DBD is 0 V. At the walls, argon metastable quench and transform to neutral argon atoms. Argon ions also transform back to neutral argon atoms while freeing secondary electrons. Where subscript  $p$  refers to different species such as ions or neutral species, electrons,  $n$  denotes the density of species,  $\Gamma$  is the flux vector,  $v_e$  is the collision frequency,  $\gamma_p$  is the secondary emission coefficient,  $n_e$  denotes the electron density,  $n_\varepsilon$  is the electron energy density, and  $\varepsilon_p$  being the mean energy of the secondary electrons. The second term in Eq. (18) is the secondary emission energy flux.

The discharge simulations for the ring electrode geometry have been performed for both, with the flow of argon gas and the static mode. For the ring electrode geometry, the discharge simulations have been performed between time scales of a nanosecond to microsecond in a 99-time step. At the instant of discharge initiation, the simulation program stops due to the iterative algorithm of EEDF that converges. A snapshot of the meshing with a mesh area (1672 mm<sup>2</sup>) of ring electrode geometry implemented using the FEM is shown in Figure 4. The separation of space charge is resolved using the boundary layer meshing on the plasma volume. The snapshots presented in Figures 5, 6, 9, 10, 13, and 14 only depict the values of electron density, electron temperature, and electrical potential at the instant of discharge initiation only as the iterative algorithm of COMSOL Multiphysics software stops at the instant of discharge and cannot illustrate 2 or more order variance in parameter values in a single snapshot.

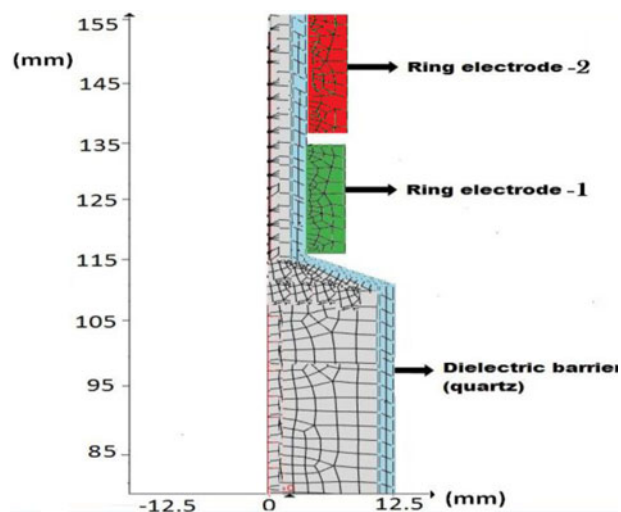


Fig. 4. The meshing of ring electrode-based APPJ using FEM.

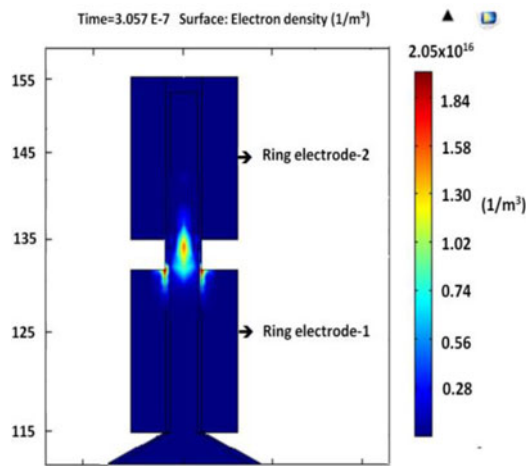


Fig. 5. Electron density at 4.5 kV/25 kHz (static condition).

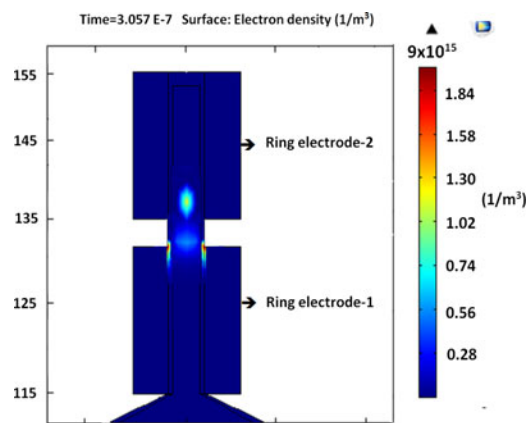


Fig. 6. Electron density at 4.5 kV/25 kHz (with flow).

**Results and discussion**

*Results of simulation*

In the preliminary set of simulations, supply frequency is increased from 10 to 25 kHz, whereas the supply voltage was fixed at 4.5 kV to understand its influence on plasma parameters. The distribution of density of electrons at the instant of the breakdown of Ar gas in a static mode and with the flow of Ar gas is represented in Figures 5 and 6.

The variation of electron density as the supply frequency is varied from 10 to 25 kHz is shown in Figure 7.

Figure 7 represents the variation of electron density values obtained for a change of supply frequency from 10 to 25 kHz at 4.5 kV. Figure 7 depicts that electron density rises with an increment of the supply frequency. However, it should be noted from Figures 5 and 6 that the electron density (static condition) is greater than electron density (With flow). Further, the electron density in the static mode is considerably greater in comparison to the electron density in the with flow condition. It is clearly seen from Figure 7 that for all supply frequencies, the electron density values in static condition is higher in comparison to with flow of gas. This primarily as a result of higher collision rate between argon atoms in static condition in comparison to with flow of gas (Raizer, 1991).

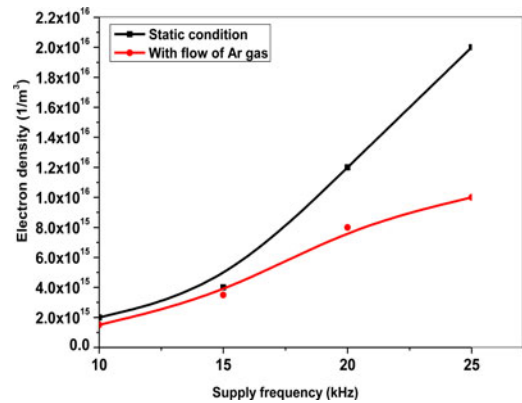


Fig. 7. Electron density versus supply frequency at 4.5 kV.

It is intriguing to note that the electron density growth is notably greater at higher supply frequency (25 kHz). This is because the electrons have lesser transit time (i.e., ~40 μs) subsequently resulting in ion buildup causing increased power consumption by ring electrode configuration. This rise in power consumption by the plasma at higher frequencies is supported from the experimental results of DBD-based argon plasma jet (see Table 1) that indicates that power consumed by the plasma has risen from 0.46 W at 4.5 kV/10 kHz to 0.88 W at 4.5 kV/25 kHz (Divya Deepak *et al.*, 2016).

In Figure 8, the supply frequency is kept constant at 25 kHz and the supply voltage has been varied from 3.5 to 6 kV, the corresponding values of electron density were noted for both conditions (with the flow of Ar gas and static mode). It is seen that electron density increases with increment in the value of supply voltage this phenomenon occurs as energetic electrons which are already available cause electron avalanche. At lower values of supply voltage, that is, 3.5 kV, the electron density in both cases (with flow and static mode) are having lower values as the seed electrons are not energetic enough to cause further secondary ionization, whereas, at higher supply voltage (6 kV), the electron density in static mode is greater in comparison to with flow of Ar gas due to the numerous collisions between them that happen in static mode (see Fig. 8).

Further, it has been observed from experimental results depicted in Table 1 when the supply voltage is increased more than 5.5 kV, the power consumed by the plasma reduces as energetic electrons cause sufficient secondary ionization of argon atoms to sustain the plasma discharge, this fact is closely in agreement with the simulation results described in Figure 8 that shows highest electron density of  $2.25 \times 10^{16} \text{ m}^{-3}$  which signifies that degree of ionization is considerably higher for sustaining the argon cold plasma.

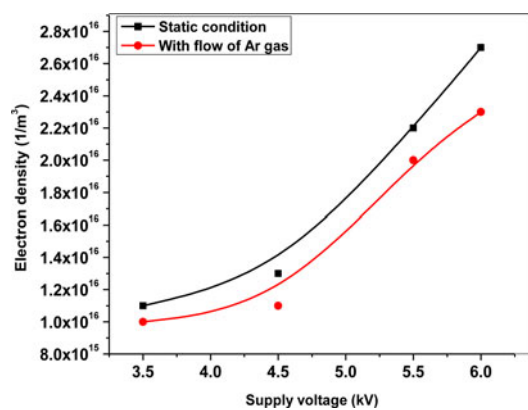
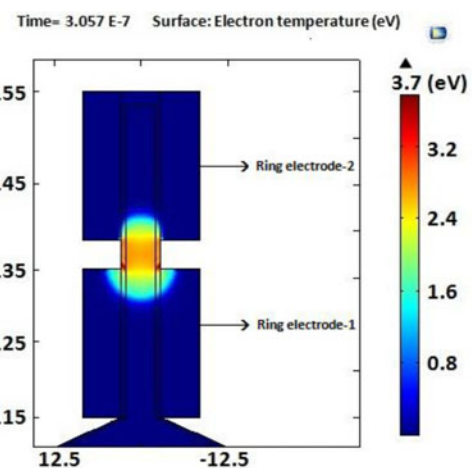
Figures 9 and 10 depict the electron temperature distribution at the moment of the breakdown of Ar gas in static condition and with the flow at 4.5 kV/25 kHz. It is evident that at all supply frequencies, the electron temperature under static condition is greater than electron temperature with flow condition. This happens as more electrons are available in static discharge mode causing more collisions between them resulting in greater energy exchange between them resulting in higher electron temperature (Raizer, 1991). But, it is further observed that as the supply frequency is increased to 20–25 kHz, then the electron temperature rises significantly as compared to lower supply frequency (10–15 kHz), this phenomenon is due to ion buildup that causes more input power to be absorbed by the electrons.

**Table 1.** Experimental results of DBD-based argon cold plasma jet (Divya Deepak et al., 2016)

Supply voltage (kV)	Supply frequency (kHz)	Peak discharge current (mA)	Jet length (mm) with sleeve	Jet length (mm) without sleeve	Power (W)
3.5	10	152	5	2	0.28
4	10	160	7	4	0.33
4.5	10	176	9	7	0.46
5	10	144	15	12	0.46
5.5	10	176	21	15	0.56
6	10	192	22	17	0.42
3.5	15	96	7	4	0.33
4	15	112	9	6	0.58
4.5	15	152	12	8	0.58
5	15	144	17	14	0.69
5.5	15	176	23	18	0.78
6	15	232	24	20	0.63
3.5	20	88	10	6	0.59
4	20	128	12	8	0.73
4.5	20	112	15	12	0.82
5	20	152	22	18	1.12
5.5	20	168	25	20	1.04
6	20	184	27	22	0.72
3.5	25	88	12	8	0.94
4	25	96	14	11	0.89
4.5	25	152	17	12	0.88
5	25	128	25	22	0.97
5.5	25	144	28	24	1.27
6	25	216	29	25	1.04

This increase in power consumed by the argon cold plasma can be seen from Table 1 where power consumed has risen from 0.82 W at 4.5 kV/20 kHz to 0.88 W at 4.5 kV/25 kHz. The seed electrons absorb energy that is accountable for further ionization of argon atoms and henceforth ensuing in the avalanche process. Subsequently, there is a growth in electron density and possibly the growth of luminous spots at cathode at supply

frequencies of 15–25 kHz as described elsewhere (Raizer, 1991). It is additionally seen from Figure 7 that the electron density rises with increment in the frequency of supply, this phenomenon occurs as the already available energetic electrons cause further ionization of argon atoms. Since the density of electrons is

**Fig. 8.** Electron density versus supply voltage at 25 kHz.**Fig. 9.** Electron temperature at 4.5 kV/25 kHz (static discharge condition).

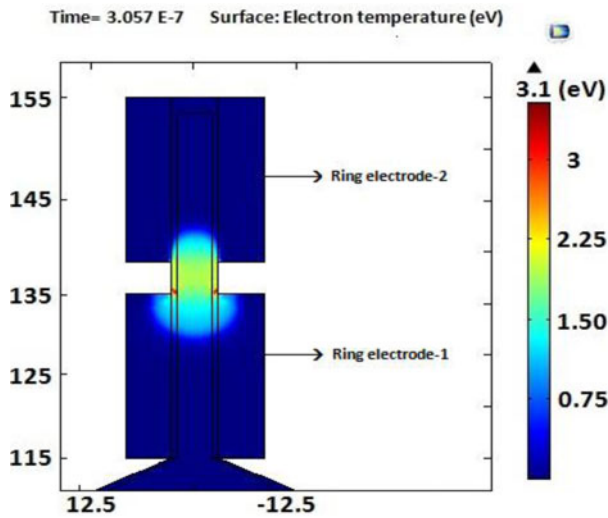


Fig. 10. Electron temperature at 4.5 kV/25 kHz (with flow condition).

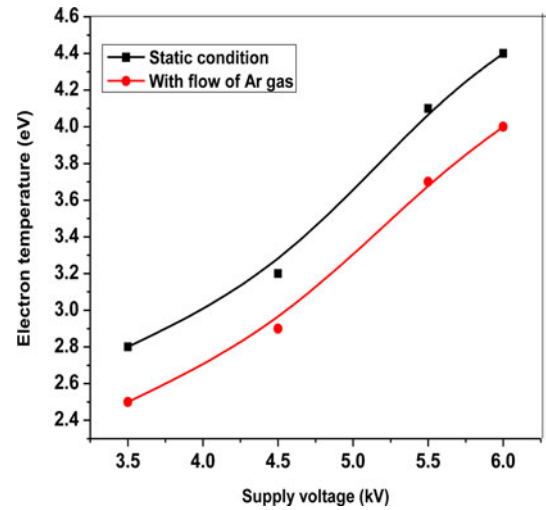


Fig. 12. Electron temperature versus supply voltage at 25 kHz.

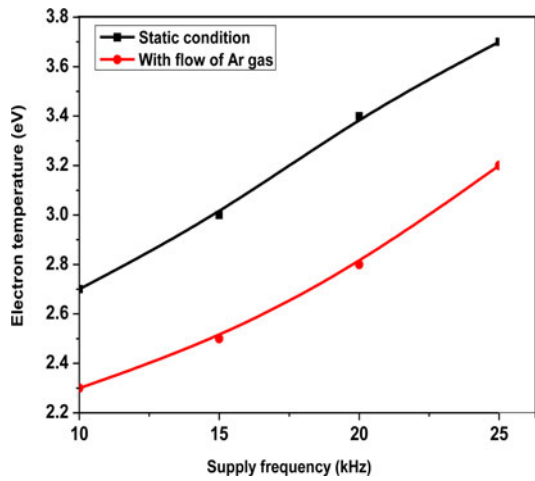


Fig. 11. Electron temperature versus supply frequency at 4.5 kV.

comparatively less in with flow condition in comparison to static mode henceforth the energy exchanged also less between them, thereby resulting in low values of electron temperature. The relationship between supply frequency and electron temperature for the developed ring electrode geometry is shown in Figure 11 which depicts that the electron temperature rises with increment in supply frequency in both static mode and with the flow of Ar gas. The electron temperature is a function of mean electron energy, it relies on electron energy density and density of electrons.

Figure 12 represents the variation of electron temperature with supply voltage at  $f = 25$  kHz. It has been observed from experimental results depicted in Table 1 when the supply voltage is increased more than 5.5 kV, the power consumed by the plasma reduces as energetic electrons cause sufficient secondary ionization of argon atoms to sustain the plasma discharge, this fact is closely in agreement with the simulation results described in Figure 8 that shows highest electron density of  $2.6 \times 10^{16} \text{ m}^{-3}$  which signifies that degree of ionization is considerably higher for sustaining the argon cold plasma.

Figures 13 and 14 represent the electrical potential that is around 1.1 kV at the instant of discharge initiation which seems

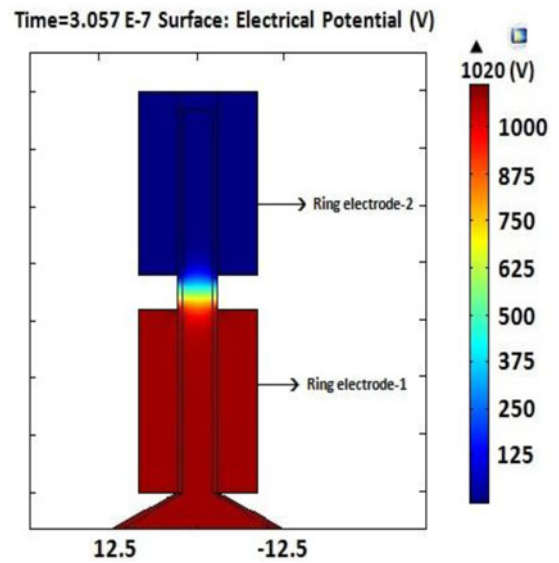


Fig. 13. Electrical potential at 4.5 kV/25 kHz (with flow).

to be relatively lower than the experimental conditions. The simulated plasma potential in COMSOL Multiphysics stops at the moment of the breakdown of Argon gas (i.e., discharge initiation) due to its iterative algorithm that converges, henceforth, it is not able to attain the values of the electrical potential of the experimental condition.

However, from the experimental results of Divya Deepak *et al.* (2016), it can be noted that initiation of discharge happens at nearly 1.02 kV (see Fig. 15) where the discharge current begins flowing. This result is closely identical with the simulation results of electrical potential with the flow of Argon gas in Figure 13. Moreover, the corresponding electron density with the flow of Argon gas is  $9 \times 10^{15} / \text{m}^{-3}$  (see Fig. 6) which shows discharge initiation. Henceforth, our result of the simulation is in agreement with the experimental results (Divya Deepak *et al.*, 2016). From Figures 13 and 14, it can be observed that the electrical potential is ensuing from ring electrode-1 to ring electrode-2 at 4.5 kV/25 kHz at the condition with the flow of Ar gas and static condition.

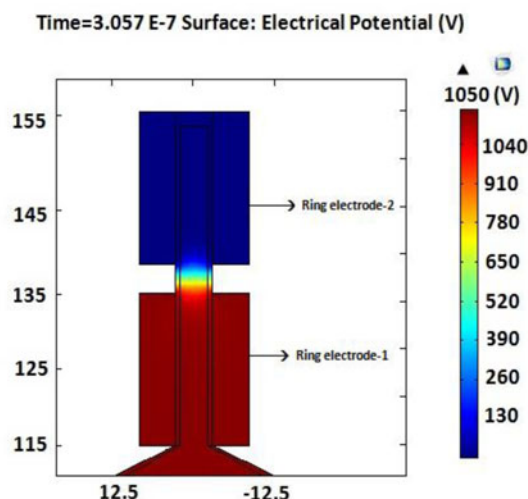


Fig. 14. Electrical potential at 4.5 kV/25 kHz (static condition).

The relationship between supply frequency and electrical potential at fixed applied voltage 4.5 kV is shown in Figure 15.

The variation of electrical potential with supply frequency at 4.5 kV is shown in Figure 16. It is clear now that at lower supply frequencies, the electrical potential reached for discharge initiation is identical for both static mode and with the flow of gas. Consequently, at a supply frequency of 10 kHz, the electrical potential desirable for discharge initiation is nearly at the same voltage level for both cases of with flow of Ar gas and in static modes. At these low supply frequencies, the electrons tend to have a higher transit time of  $\sim 100 \mu\text{s}$ . Nevertheless, at a supply frequency of 20–25 kHz, the electrons possess lesser transit time  $\sim 40 \mu\text{s}$  owing to ion buildup, so the electrical potential reached for discharge initiation is becoming noticeable which may also result in additional power consumption.

### Summary

From our simulation results at 4.5 kV and different supply frequencies, it is observed that electron density grows with supply frequency for both (with the flow of argon gas and static

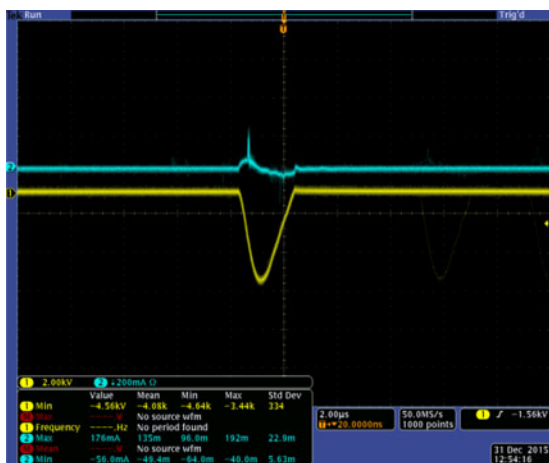


Fig. 15. V-I characteristics at 4.5 kV/25 kHz (argon cold plasma jet) (Divya Deepak *et al.*, 2016).

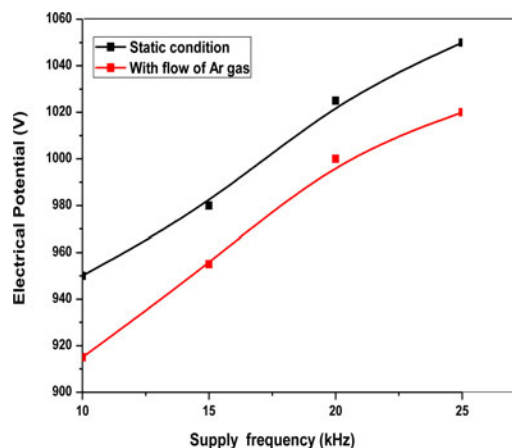


Fig. 16. Electrical potential versus supply frequency at 4.5 kV.

condition). However, it is observed that electron density is comparatively higher in the case of the static condition of argon gas than with flow at all supply frequencies since more argon atoms are available for ionization (see Figs 5 and 6). With the increment of supply frequency in both conditions of with flow of argon gas and static mode, the electron temperature rises (see Fig. 7). From the simulation results at  $f = 25 \text{ kHz}$  and different supply voltages, it is seen from Figure 8 that electron density rises with increment in supply voltages. This is because at higher supply voltages, the initially available seed electrons absorb additional energy resulting in electrons that are energetic which causes further ionization of argon atoms.

But it is noted that the electron temperature is more for static condition compared to with flow of argon gas (see Figs 9 and 10) as the particle density is lesser in case of with flow of argon. Thus, lesser collisions and lesser energy exchange (between electrons and argon atoms) in case of with flow of gas which results in lower electron density and lower electron temperature compared to static discharge condition. Further, the electron temperature rises with increment in supply frequency in both static mode and with the flow of Ar gas (see Fig. 11). Also, electron temperature also increases with an increase in supply voltage. It is observed that when the supply voltage is incremented more input power is dumped into the plasma resulting in more energetic electrons being available to cause secondary ionization (see Fig. 12).

Electrical potential rises with increment in supply frequency as more input power is dumped into the plasma as supply frequency increases. It is observed that electrical potential reached is less in the case of with flow of argon gas in comparison to the static mode of discharge (see Fig. 16).

It is also observed that the simulation data has been closely in agreement with the experimental results (Divya Deepak *et al.*, 2016) depicted in Table 1 where the rise in power consumed by the argon cold plasma from 0.46 W at 4.5 kV/10 kHz to 0.88 W at 4.5 kV/25 kHz has been justified with Figure 7 which clearly depicts the growth in electron density due to ion buildup that resulting in more consumption of input power. Also, from Figure 11, the increase in electron temperature at higher supply frequencies (20–25 kHz) due to more power absorbed the seed electrons is justified with the experimental results in Table 1 that clearly indicate that power consumed by the argon plasma increased from 0.82 W at 4.5 kV/20 kHz to 0.88 W at 4.5 kV/25 kHz.



Further, it has been observed from experimental results depicted in Table 1 that when the supply voltage is increased more than 5.5 kV, the power consumed by the plasma reduces as energetic electrons cause sufficient secondary ionization of argon atoms to sustain the plasma discharge, this fact is closely in agreement with the simulation results described in Figure 8 that shows highest electron density of  $2.6 \times 10^{16} \text{ m}^{-3}$  which signifies that degree of ionization is considerably higher for sustaining the argon cold plasma.

It is imperative to further note that the discharge initiation in the argon plasma occurs at 1.02 kV at 4.5 kV/25 kHz which closely matches the simulation results depicted in Figure 13 where the electrical potential is 1.02 kV.

These simulation and experimental results of DBD-based argon cold plasma jet would be useful for designing and operating ring electrode configuration without any arcing phenomenon. Further, the DBD-based argon cold plasma jet could be used for various biomedical applications. However, this will require *in vitro* biomedical laboratory testing and study of biomedical changes and other sterilizing effects to establish the relevance.

**Acknowledgment.** The Director, CSIR-Central Electronics Engineering Research Institute, Pilani is gratefully acknowledged for providing necessary lab facilities in performing these experiments

## References

- Becker KH, Schoenbach KH and Eden JG (2006) Microplasmas and applications. *Journal of Physics D: Applied Physics* **39**, R55.
- Benhansour M, Nikravech M, Morvan D, Amouroux J and Chapelle J (2004) Diagnostic by emission spectroscopy of an argon-hydrogen RF inductive thermal plasma for purification of metallurgical grade silicon. *Journal of Physics D: Applied Physics* **37**, 2966.
- Chirokov A, Gutsol A and Fridman A (2005) Atmospheric pressure plasma of dielectric barrier discharges. *Pure and Applied Chemistry* **77**, 487.
- Deng XT, Shzi JJ, Shama and Kong MG (2005) Effects of microbial loading and sporulation temperature on atmospheric plasma inactivation of *Bacillus subtilis* spores. *Applied Physics Letters* **87**, 153901.
- Divya Deepak G, Joshi NK, Pal U and Prakash R (2016) Electrical characterization of atmospheric pressure dielectric barrier discharge-based cold plasma jet using ring electrode configuration. *Laser and Particle Beams* **34**, 615.
- Divya Deepak G, Joshi NK, Kumar Pal D and Prakash R (2017) A low power miniaturized dielectric barrier discharge based atmospheric pressure plasma jet. *Review of Scientific Instruments* **88**, 013505.
- Divya Deepak G, Joshi NK and Prakash R (2018a) Model analysis and electrical characterization of atmospheric pressure cold plasma jet in pin electrode configuration. *AIP Advances* **8**, 055321.
- Divya Deepak G, Joshi NK, Prakash R and Pal U (2018b) Electrical characterization of argon and nitrogen based cold plasma jet. *The European Physical Journal Applied Physics* **83**, 20801.
- Duan Y, Huang C and Yu Q (2005) Low-temperature direct current glow discharges at atmospheric pressure. *IEEE Transactions on Plasma Science* **33**, 328.
- Eliasson B and Kogelchitz U (1991) Modeling and applications of silent discharge plasmas. *IEEE Transactions on Plasma Science* **19**, 309.
- Frame JW, Wheeler DJ, Detemple TA and Eden JG (1997) Microdischarge devices fabricated in silicon. *Applied Physics Letters* **71**, 1165.
- Gadkari S, Tu X and Gu S (2017) Fluid model for a partially packed dielectric barrier discharge plasma reactor. *Physics of Plasmas* **24**, 093510.
- Hagelaar GJM and Pitchford LC (2005) Solving the Boltzmann equation to obtain electron transport coefficients and rate coefficients for fluid models. *Plasma Sources Science and Technology* **14**, 722.
- Hongtao YC and Uhm HS (2006) Microplasma jet at atmospheric pressure. *Applied Physics Letters* **89**, 221504.
- Jeong JY, Babayan SE, Tu VJ, Park J, Henins I, Hicks RF and Selwyn GS (1998) Etching materials with an atmospheric-pressure plasma jet. *Plasma Sources Science and Technology* **7**, 282.
- Joh HM, Kang H, Chung TH and Kim S (2014) Electrical and optical characterization of atmospheric-pressure helium plasma jets generated with a pin electrode: effects of the electrode material, ground ring electrode, and nozzle shape. *IEEE Transactions on Plasma Science* **42**, 3656.
- Kelly S and Turner M (2011) Fluid model of the 2D cross section of an AC driven plasma at atmospheric pressure 2011. In *Proceeding of 30th International Conference on Phenomenon in Ionized Gases, National Centre for Plasma Science and Technology*, Belfast UK, 28 August – 2 September 2011, Topic number B5.
- Kim H, Brockhaus A and Engemann J (2009) Atmospheric pressure argon plasma jet using a cylindrical piezoelectric transformer. *Applied Physics Letters* **95**, 211501.
- Kim K, Kim G, Hong YC and Yang SS (2010) A cold micro plasma jet device suitable for bio-medical applications. *Microelectronic Engineering* **87**, 1177.
- Kruger CH, Owano TG and Laux CO (1997) Experimental investigation of atmospheric pressure nonequilibrium plasma chemistry. *IEEE Transactions on Plasma Science* **25**, 1042.
- Lu XP and Laroussi M (2006) Dynamics of an atmospheric pressure plasma plume generated by submicrosecond voltage pulses. *Journal of Applied Physics* **100**, 063302.
- Lu XP, Jiang ZH, Xiong Q, Tang ZY, Hu XW and Pan Y (2008) An 11 cm long atmospheric pressure cold plasma plume for applications of plasma medicine. *Applied Physics Letters* **92**, 081502.
- Naidis GV (2012) Modeling of helium plasma jets emerged into ambient air: influence of applied voltage, jet radius, and helium flow velocity on plasma jet characteristics. *Journal of Applied Physics* **112**, 103304.
- Nie QY, Ren CS, Wang DZ and Zhang JL (2008) A simple cold Ar plasma jet generated with a floating electrode at atmospheric pressure. *Applied Physics Letters* **93**, 011503.
- Pal UN, Gulati P, Kumar N, Prakash R and Srivastava V (2012) Multiswitch equivalent electrical model to characterize coaxial DBD tube. *IEEE Transactions on Plasma Science* **40**, 1356.
- Radu I, Bartnikas R, Czeremuszkin G and Wertheimer MR (2003) Diagnostics of dielectric barrier discharges in noble gases: atmospheric pressure glow and pseudoglow discharges and spatio-temporal patterns. *IEEE Transactions on Plasma Science* **31**, 411.
- Raizer YP (1991) *Gas Discharge Physics*. Berlin, Germany: Springer-Verlag, p. 172.
- Roth JR, Nourgostar S and Bonds T (2007) The one atmosphere uniform glow discharge plasma (OAUGDP)—a platform technology for the 21st century. *IEEE Transactions on Plasma Science* **35**, 233.
- Sakiyama Y and Graves DB (2006) Corona-glow transition in the atmospheric pressure RF-excited plasma needle. *Journal of Physics D: Applied Physics* **39**, 3644.
- Schutze, Jeong JY, Babayan SE, Park JY, Selwyn GS and Hicks RF (1998) The atmospheric-pressure plasma jet: a review and comparison to other plasma sources. *IEEE Transactions on Plasma Science* **26**, 1685.
- Selwyn GS, Herrmann HW, Park J and Henins I (2001) Materials processing using an atmospheric pressure, RF-generated plasma source. *Contributions to Plasma Physics* **41**, 610.
- Shashurin A and Keidar M (2015) Experimental approaches for studying non-equilibrium atmospheric plasma jets. *Physics of Plasmas* **22**, 122002.
- Sladek REJ, Stoffels E, Walraven R, Tielbeek PEA and Koolhoven RA (2004) Plasma treatment of dental cavities: a feasibility study. *IEEE Transactions on Plasma Science* **32**, 1540.
- Stoffels E, Flikweert AJ, Stoffels WW and Kroesen GMW (2002) Plasma needle: a non-destructive atmospheric plasma source for fine surface treatment of (bio) materials. *Plasma Sources Science and Technology* **11**, 383.
- Stoffels E, Kieft IE and Sladek REJ (2003) Superficial treatment of mammalian cells using plasma needle. *Journal of Physics D* **37**, 2966.
- Tendero C, Tixier C, Tristant P, Desmaison J and Leprince P (2006) Atmospheric pressure plasmas: a review. *Spectrochimica Acta Part B: Atomic Spectroscopy* **61**, 2.
- Teschke M, Kedzierski J, Finantu-Dinu E, Korzec D and Engemann J (2005) High-speed photographs of a dielectric barrier atmospheric pressure plasma jet. *IEEE Transactions on Plasma Science* **33**, 310.

- Walsh JL, Shi JJ and Kong MG** (2006) Contrasting characteristics of pulsed and sinusoidal cold atmospheric plasma jets. *Applied Physics Letters* **88**, 171501.
- Xu X** (2001) Dielectric barrier discharge — properties and applications. *Thin Solid Films* **390**, 237.
- Xu GM, Ma Y and Zhang GJ** (2008) DBD plasma jet in atmospheric pressure argon. *IEEE Transactions on Plasma Science* **36**, 1352.
- Yi H, Lu NA, Jing P, Jie L and Yan W** (2013) Discharge characteristics of an atmospheric pressure argon plasma jet generated with screw ring-ring electrodes in surface dielectric barrier discharge. *Plasma Science and Technology* **15**, 780.